ChemComm

COMMUNICATION

View Article Online
View Journal | View Issue

Cite this: *Chem. Commun.*, 2026, 62, 4778

Received 30th October 2025,
Accepted 19th January 2026

DOI: 10.1039/d5cc06127j

rsc.li/chemcomm

Atomically thin boron nitride nanosheets assembled on three-dimensional NiFe-layered double hydroxide for enhanced oxygen evolution reaction

Chunbo Zhu,†[ab] Jiahui Lu,†[ac] Chenxi Wang,[ac] Mingyang Xia,[ac] Sheng Hu*[abcd] and Yang Cao *[abcd]

Atomically thin hexagonal boron nitride (BN) crystals as efficient co-catalysts can enhance both the activity and stability of electrochemical oxygen evolution reactions. However, their practical use has been limited by the existing assembly methods incompatible with complex three-dimensional electrocatalysts. In this work, we develop an electrophoretic deposition strategy to firmly attach liquid-exfoliated BN nanosheets onto nanostructured NiFe-layered double hydroxide (LDH) electrodes, achieving a current density of 1000 mA cm^{-2} at an overpotential of 318 mV and maintaining stability for over 240 h. This work provides a feasible approach for integrating BN nanosheets into electrocatalytic systems, extendable to other low-dimensional materials.

Electrochemical water splitting is a clean method for hydrogen production, but the anodic oxygen evolution reaction (OER) remains kinetically sluggish due to its four-electron process, requiring high overpotentials.[1] High-activity catalysts often rely on oxidative metal sites[2] or defects,[3–5] which may cause dynamic changes in reactive sites or even irreversible structural damage. Although protective coatings improve stability,[6] they seldom enhance activity. Recent advances using core–shell structures,[7] and high-entropy alloys[8] have improved both activity and stability through tailored structures and synergy. However, under harsh OER conditions, active species still tend to degrade. Encapsulation with ultrathin two-dimensional (2D) materials[9,10] offers a promising solution. For example, a van der Waals–heterostructure of monolayer hexagonal boron nitride (hBN) on NiFe (oxy)hydroxide significantly boosted OER current density and stability.[11] The atomically thin hBN provides adsorption sites and protects active centers without blocking charge transfer. However, such monolayers are typically synthesized *via* chemical vapor deposition and transferred to flat substrates, limiting application to practical high-surface-area catalysts with three-dimensional (3D) nanoporous architectures.[12,13] The roughness of these 3D substrates exceeds the atomic thickness of monolayer hBN, hindering effective van der Waals integration. Thus, developing methods to assemble 2D hBN co-catalysts onto complex 3D-structured electrodes is crucial for advancing OER performance.

In recent years, liquid-phase exfoliation methods have been reported for preparing atomically thin boron nitride nanosheets (BNNS), achieving large-scale production and stable dispersion.[14] On the one hand, the surface of BNNS is usually decorated with functional groups,[15,16] or engages in π–π interactions with tannic acid (TA),[17] which can facilitate exfoliation and assembly with other materials. BNNS self-assembled on CdS nanorods through chemical adsorption, forming a 5–10 nm compact shell,[18] thereby enhancing photocatalytic activity and stability. On the other hand, the charging of BNNS further allows their effective deposition on target substrates driven by an external electrical field.[19,20] For example, micron-thick BNNS coatings have been electrophoretically deposited (EPD) on Cu to prevent electrochemical corrosion in a marine environment.[21] However, in these cases, the inert BNNS layer is compact and thick, leading to high interfacial resistance that impedes charge transfer, making it unsuitable for electrocatalytic applications.

Inspired by these insights, we designed our catalyst by assembling BNNS exfoliated in the liquid phase onto 3D nanoporous NiFe-layered double hydroxide (LDH) *via* EPD, to simultaneously improve catalytic activity and durability. The optimized BNNS/NiFe-LDH composite electrode achieves enhanced OER performance compared to NiFe-LDH. Combining a methanol oxidation probe experiment and *in situ* Raman spectroscopy, we reveal that the BNNS layer has strong adsorption affinity toward *OH species, promoting the adsorption of OER intermediates

[a] *State Key Laboratory of Physical Chemistry of Solid Surfaces, Collaborative Innovation Center of Chemistry for Energy Materials (iChEM), Xiamen University, Xiamen, 361005, China. E-mail: sheng.hu@xmu.edu.cn, yangcao@xmu.edu.cn*
[b] *Pen-Tung Sah Institute of Micro-Nano Science and Technology, Xiamen University, Xiamen, 361005, China*
[c] *College of Chemistry and Chemical Engineering, Xiamen University, Xiamen, 361005, China*
[d] *Innovation Laboratory for Sciences and Technologies of Energy Materials of Fujian Province (IKKEM), Xiamen, 361005, China*
† Equal contribution.

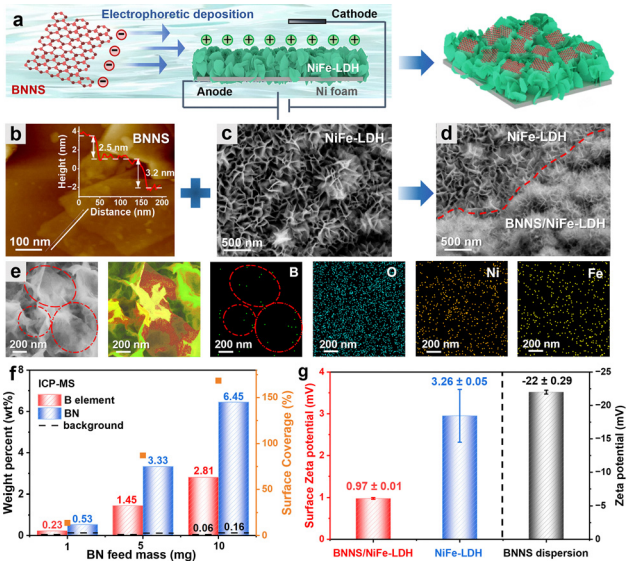

Fig. 1 (a) Schematic illustration of the electrophoretic deposition process to load BNNS on NiFe-LDH. (b) AFM characterization of BNNS on Si substrate; scale bar: 100 nm; inset showing the thickness profile. SEM images of (c) NiFe-LDH and (d) BNNS/NiFe-LDH (the region below the red dashed line); scale bar: 500 nm. (e) High-resolution SEM image showing the morphology of BNNS, corresponding false-color SEM image and EDS elemental mapping. (f) B and BN contents of BNNS/NiFe-LDH synthesized with different BN feed masses, determined by ICP-MS, background signals (black dashed lines) from possible BNNS adsorption from the electrolyte. (g) Surface zeta potential of BNNS/NiFe-LDH, NiFe-LDH, together with the zeta potential of 1 mg mL^{-1} BNNS dispersion.

and the formation of active oxygen species. Notably, a six-fold enhancement in stability at 1 A cm^{-2} is achieved. Inductively coupled plasma mass spectrometry (ICP-MS) analysis verifies that BNNS encapsulation significantly inhibits the detachment of NiFe-based metal catalysts. This study demonstrates that integration of 2D BNNS through EPD enables both improved OER activity and stability, offering perspectives in electrochemical applications of atomically thin BNNS.

Fig. 1 illustrates the synthesis and structural characterizations of our OER anodes. The BNNS were exfoliated *via* tannic-acid-assisted wet ball milling.[17] The preparation conditions are systematically optimized, achieving a maximum yield of 14 wt% (*i.e.*, the mass fraction of exfoliated BNNS to the raw material, Fig. S1). The resulting BNNS remain well dispersed in deionized water for over one month (Fig. S2a). Statistical analysis of 20 nanosheets using atomic force microscopy (AFM, Fig. 1b) and electron microscopy (SEM, Fig. S2b) shows that the thickness of the nanosheets is 3.5 ± 1.5 nm, with a lateral size of about 350 ± 150 nm (Fig. S2c). The X-ray diffraction (XRD) technique shows a characteristic peak at 26.9° assigned to the hBN (002) plane.[14] These results indicate that atomically thin BNNS were successfully fabricated. Then, EPD was performed in a two-electrode system (Fig. 1a). Under a positive potential, the negatively charged BNNS migrated toward the electrode and were uniformly assembled onto the formerly electrodeposited NiFe-LDH nanoflowers (Fig. 1c) on Ni foam *via* electrostatic adsorption (see details in 'Samples fabrication' and Fig. S3 in SI). The slightly altered surface contrast at the BNNS-modified areas suggests the effectiveness of the EPD, and can be attributed to the insulating nature of hBN (Fig. 1d and Fig. S4). High-resolution SEM images further show the presence of hBN nanosheets (Fig. 1e and Fig. S5). The BNNS coverage is around 87%, as estimated. The corresponding energy dispersive spectrometry (EDS) further confirms the locally enriched boron signals corresponding to BNNS regions. To quantify the incorporation of BNNS, we used concentrated nitric acid for digestion and ICP-MS analysis,[22] and found an increased hBN content with the initial BN feed mass for EPD (Fig. 1f); see details in 'B and BN content calculations' and Table S1 in SI. Therefore, the EPD process enables controllable and efficient BNNS assembly. The successful assembly of BNNS was further confirmed by zeta potential measurements, where the zeta potential of pristine NiFe-LDH (+3.2 ± 0.05 mV, consistent with values in the literature[23]) decreased to +0.97 ± 0.01 mV after the introduction of negatively charged BNNS (−22 ± 0.29 mV), as shown in Fig. 1g. This can be attributed to the adsorption of oxygen-based moieties on the BNNS surface, including hydroxyl group species and phenolic hydroxyl groups on TA introduced during exfoliation.[17,24]

Electrochemical measurements were carried out in a typical three-electrode configuration in 1 M KOH solution. Under optimized EPD conditions of 0.1 V and 0.5 C cm^{-2}, and a BNNS concentration of 0.1 mg mL^{-1}, the resulting electrode showed the best OER performance (Fig. S6). Linear sweep voltammetry (LSV) curves (Fig. 2a) demonstrate that the optimal BNNS/NiFe-LDH exhibits improved OER overpotentials of 210, 268 and 318 mV at current densities of 100, 500 and 1000 mA cm^{-2}, respectively, whereas NiFe-LDH requires 262, 316 and 377 mV under the same conditions. Due to the variations in activity (Fig. S7), the highest-performing BNNS/NiFe-LDH and NiFe-LDH were compared. The former also maintains superior performance in weakly alkaline

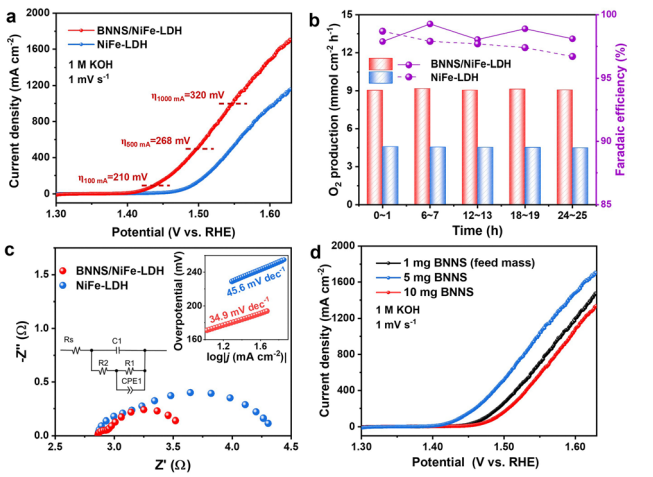

Fig. 2 (a) LSV curves of BNNS/NiFe-LDH and NiFe-LDH in 1 M KOH solution at a scan rate of 1 mV s^{-1} with 90% *iR* correction, with overpotentials at various representative current densities marked. (b) O_2 yield and corresponding faradaic efficiency measured in 1-hour intervals every 5 hours within the first 25 hours (at 1.55 V *vs.* RHE). (c) Electrochemical impedance spectroscopy. Inset: Tafel slope. (d) BNNS feed mass-dependent LSV curves.

and neutral electrolytes (Fig. S8). Oxygen evolution was quantified at 1.55 V (*vs.* reversible hydrogen electrode, RHE) using a laboratory-built flowmeter. As shown in Fig. 2b, BNNS/NiFe-LDH generates nearly twice the amount of O_2 compared to NiFe-LDH, with a more stable faradaic efficiency largely exceeding 98%, indicating negligible side reactions. To further investigate the reaction kinetics, we plotted the Tafel slope of BNNS/NiFe-LDH, which is 34.9 mV dec^{-1}, lower than that of 45.6 mV dec^{-1} for NiFe-LDH (Fig. 2c, inset). In addition, electrochemical impedance spectroscopy was also performed at 1.53 V (*vs.* RHE) (Fig. 2c), where BNNS/NiFe-LDH has a smaller semicircle in the Nyquist plot, corresponding to lower charge transfer resistance.[25] Based on the LSV curves of samples fabricated *via* EPD with different BNNS feed mass loadings (Fig. 2d), the optimal loading capacity is achieved with the addition of 5 mg of BNNS, corresponding to a concentration of 0.1 mg mL^{-1}. Control experiments confirmed that TA on the BNNS surface contributed negligibly to the activity (see Fig. S9 and details in Samples fabrication section in the SI). As shown in Fig. S10 and Table S2, the overpotential of BNNS/NiFe-LDH at 500 mA cm^{-2} is comparable to that of the best-performing NiFe-based electrocatalysts reported to date, together with a rival Tafel slope.

There is no significant increase in the electrochemically active surface area (ECSA) of BNNS/NiFe-LDH, as evidenced in Fig. S11. Through LSV in tetramethylammonium hydroxide[26,27] (Fig. S12), the main active sites are confirmed in NiFe-LDH. For details, please see 'Explanation of active sites' in the SI. X-ray diffraction (Fig. S13) and photoelectron spectroscopy[28] (Fig. S14 and S15) also show that the assembly of BNNS has no detectable influence on the crystallization and electronic structures of NiFe-LDH. In our methanol oxidation reaction (MOR) probe experiments,[29] as shown in Fig. 3a, after adding 1 M methanol to 1 M KOH, the increased current density for BNNS/NiFe-LDH (with respect to its OER current) is significantly larger than that of NiFe-LDH. It is known that the nucleophilic methanol molecules can directly react with the initial *OH intermediates (electron-deficient), generating an oxidation current immediately after the onset potential of the Ni(II)/Ni(III) transition.[30] For OER, our previous theoretical and experimental investigations revealed that the rate-determining step is the deprotonation process from *OH to *O.[11] Hence, the difference in current induced by MOR can serve as an indicator of the degree of *OH accumulation on the catalyst surface.[31,32] We further integrated the LSV curves into current density *versus* time for quantitative comparison. As shown in Fig. 3b, the capacitance of the effective *OH species is 85.6 C cm^{-2} for BNNS/NiFe-LDH and 13.1 C cm^{-2} for NiFe-LDH, clearly demonstrating enhanced *OH adsorption on BNNS/NiFe-LDH.

In situ Raman spectroscopy was further employed to investigate the adsorption of intermediate species. Raman spectra of BNNS/NiFe-LDH and NiFe-LDH were recorded at various potentials, each held for 30 s before measurements to ensure accuracy (Fig. 3c). From 1.26 to 1.31 V, characteristic peaks around 455 and 535 cm^{-1} correspond to Ni^{II}–O in BNNS/NiFe-LDH,[33] and the peak at around 1060 cm^{-1} corresponds to NO_3^- from electrolyte, consistent with reports in the literature.[34]

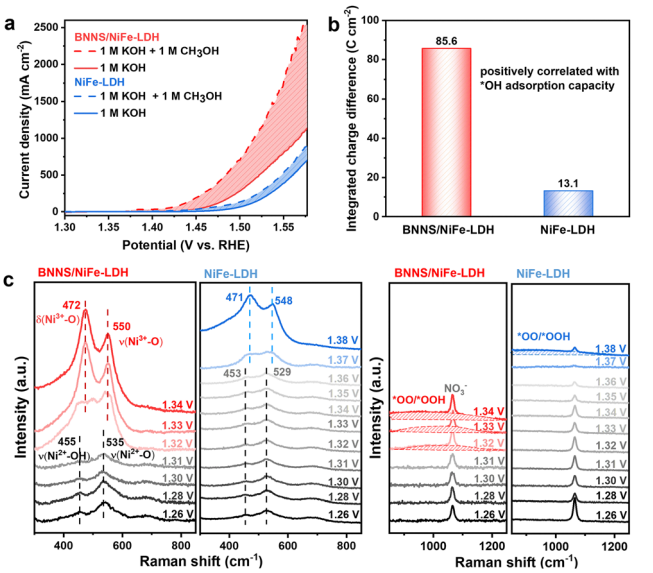

Fig. 3 (a) Polarization curves of BNNS/NiFe-LDH and NiFe-LDH in 1 M KOH solution with 1 M methanol (dashed lines) and without methanol (solid lines); scan rate: 1 mV s^{-1}. (b) Integrated charge differences between the polarization curves in the presence and absence of 1 M methanol for BNNS/NiFe-LDH and NiFe-LDH, which are positively correlated with *OH adsorption capacity. (c) *In situ* Raman spectra of BNNS/NiFe-LDH and NiFe-LDH. The wide peak at 800–1200 cm^{-1}, highlighted by the red and blue shaded areas, corresponds to the O–O stretch of active oxygen intermediates.

At 1.32 V, the two peaks of Ni^{II} disappear, and two new peaks appear at 472 and 550 cm^{-1}, representing Ni^{III}–O in the active NiOOH phase.[33,35] Simultaneously, a broad band emerges between 800 and 1200 cm^{-1}, attributed to the O–O stretch of the active oxygen species (*OH/*OOH).[36,37] This indicates that transformation of Ni species is correlated with the formation of *OOH. Notably, these spectral changes occur ~50 mV earlier in BNNS/NiFe-LDH than in NiFe-LDH, matching its advanced OER overpotential, suggesting that the incorporation of BNNS significantly accelerates the formation of active oxygen intermediates. Overall, BNNS facilitate the adsorption of *OH reactant and promote the generation of the active NiOOH phase during OER, explaining the improved catalytic performance observed for BNNS/NiFe-LDH.

The stability of BNNS/NiFe-LDH was evaluated under 1 A cm^{-2} in 1 M KOH (Fig. 4a). It exhibited a decay of only 2% over 240 h, and a faradaic efficiency of over 95% over 200 h (Fig. S16), demonstrating considerably enhanced stability. In contrast, the performance of NiFe-LDH decreased dramatically after only 35 h. Post-test characterization (Fig. 4b) shows that BNNS/NiFe-LDH retains its morphology (Fig. S17). SEM image reveals that BNNS remain on the catalyst surface due to the strong electrostatic interactions formed during the EPD process in a mixed electrolyte, whereas the NiFe-LDH catalytic layer detached, exposing the Ni foam substrate underneath. Quantitative analysis *via* ICP measurements corroborates these findings. For NiFe-LDH after the durability tests, considerably larger amounts of Ni and Fe species were dissolved in the electrolyte compared with those of BNNS/NiFe-LDH (Fig. 4c). Details are given in the SI, Tables S3

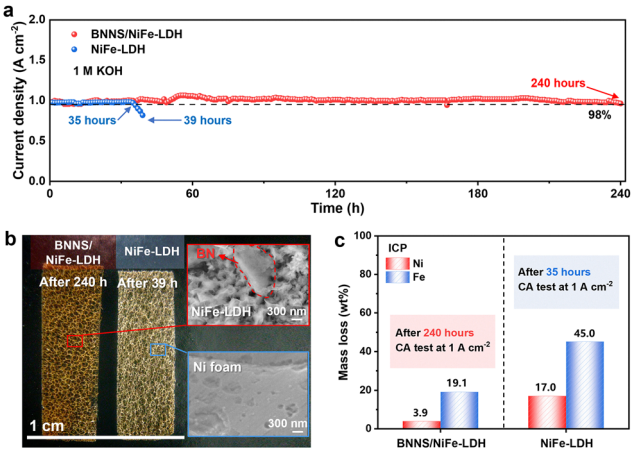

Fig. 4 (a) Chronoamperometric (CA) curves of BNNS/NiFe-LDH and NiFe-LDH at 1 A cm^{-2}. (b) Photographs and SEM images (scale bar: 300 nm) of the two catalysts after respective CA tests. BNNS, highlighted within the red dashed box, remain anchored on the surface. (c) Mass loss of metallic elements in BNNS/NiFe-LDH and NiFe-LDH after respective CA tests.

and S4. Therefore, the dramatic improvement in stability may be generated from direct encapsulation by BNNS, which effectively suppresses metal leaching and prevents the detachment of catalysts during OER.

To summarize, we developed a strategy of depositing 2D nanosheet-based co-catalysts onto complex 3D nanocatalysts. Beyond the Ni foam substrate, we also show the possibility of depositing BNNS on carbon paper for improved catalytic activity (Fig. S18). The synthesized BNNS/NiFe-LDH composite catalysts outperform pristine NiFe-LDH. The balance of enhanced activity and durability is attributed primarily to the role of atomically thin BNNS in optimizing *OH adsorption at the electrochemical interface, while effectively suppressing metal dissolution. Together with the liquid exfoliation technique that allows the mass production of hBN crystals, our results present BNNS as potential candidates for 2D co-catalysts. This scalable approach, demonstrated by an electrode of 10 cm × 8 cm (Fig. S17), holds great potential for large-scale practical applications.

Conflicts of interest

There are no conflicts to declare.

Data availability

The data supporting this article have been included as part of the supplementary information (SI). Supplementary information: experimental details, ICP data, *etc.* See DOI: https://doi.org/10.1039/d5cc06127j.

Acknowledgements

We thank Youchao Liu, Yingru Qiu, Xin Weng, Xin Zhang, Huaixin Li, and Lihao Wang for their technical assistance and support.

References

1 J. H. Shah, Q. X. Xie, Z. C. Kuang, R. L. Ge, W. H. Zhou, D. R. Liu, A. I. Rykov, X. N. Li, J. S. Luo and J. H. Wang, *J. Electrochem.*, 2022, **28**, 3.
2 Q. B. Wu, J. W. Liang, M. J. Xiao, C. Long, L. Li, Z. H. Zeng, A. Mavric, X. Zheng, J. Zhu, H. W. Liang, H. F. Liu, M. Valant, W. Wang, Z. X. Lv, J. Li and C. H. Cui, *Nat. Commun.*, 2023, **14**, 997.
3 J. Wang, H. Yang, F. Li, L. G. Li, J. B. Wu, S. H. Liu, T. Cheng, Y. Xu, Q. Shao and X. Q. Huang, *Sci. Adv.*, 2022, **8**, eabl9271.
4 J. Ran, M. Jaroniec and S.-Z. Qiao, *Adv. Mater.*, 2018, **30**, 1704649.
5 F. Z. Song, X. Ding, Y. Y. Wan, T. Zhang, G. G. Yin, J. B. Brown and Y. Rao, *J. Phys. Chem. Lett.*, 2025, **16**, 3535–3543.
6 M. Ju, Y. Zhou, F. Dong, Z. X. Guo, J. Wang and S. H. Yang, *ACS Mater. Lett.*, 2024, **6**, 3602–3624.
7 J. K. Liang, H. X. Li, L. Chen, M. N. Ren, O. A. Fakayode, J. Y. Han and C. S. Zhou, *Ind. Crop. Prod.*, 2023, **193**, 116214.
8 L. Y. Liu, X. Ding, H. T. Qin, S. Y. Tang, L. L. Xu and F. Z. Song, *Chemistry*, 2025, **7**, 190.
9 H. Liu, X. H. Zhang, Y. X. Li, X. Li, C. K. Dong, D. Y. Wu, C. C. Tang, S. L. Chou, F. Fang and X. W. Du, *Adv. Energy Mater.*, 2020, **10**, 1902521.
10 Y. X. Hao, S. F. Hung, C. Tian, L. Q. Wang, Y. Y. Chen, S. Zhao, K. S. Peng, C. C. Zhang, Y. Zhang, C. H. Kuo, H. Y. Chen and S. J. Peng, *Angew. Chem., Int. Ed.*, 2024, **63**, e202402018.
11 Y. Z. Lu, B. X. Li, N. Xu, Z. H. Zhou, Y. Xiao, Y. Jiang, T. Li, S. Hu, Y. J. Gong and Y. Cao, *Nat. Commun.*, 2023, **14**, 6965.
12 H. Lei, L. Ma, Q. X. Wan, Z. W. Huangfu, S. Z. Tan, Z. L. Wang and W. J. Mai, *Nano Energy*, 2022, **104**, 107941.
13 Y. Z. Chen, Q. H. Li, Y. X. Lin, J. Liu, J. Pan, J. G. Hu and X. Y. Xu, *Nat. Commun.*, 2024, **15**, 7278.
14 H. R. Zhao, J. H. Ding, C. C. Zhao, J. G. Wang, Y. J. Fang and J. Zhu, *ACS Sustainable Chem. Eng.*, 2023, **11**, 4633–4642.
15 S. H. Chen, R. Z. Xu, J. M. Liu, X. L. Zou, L. Qiu, F. Y. Kang, B. L. Liu and H. M. Cheng, *Adv. Mater.*, 2019, **31**, 4633–4642.
16 Z. Q. Wu, J. Dong, X. T. Li, X. Zhao, C. C. Ji and Q. H. Zhang, *Compos. Part B Eng.*, 2023, **266**, 111001.
17 N. Wu, W. Yang, S. Che, L. Sun, H. W. Li, G. Ma, Y. K. Sun, H. C. Liu, X. B. Wang and Y. F. Li, *Composites, Part A*, 2023, **164**, 107266.
18 X. Y. Fang, J. J. Wang, Y. Q. Yu, S. F. Kang and L. F. Cui, *Int. J. Hydrogen Energy*, 2020, **45**, 14841–14848.
19 K. Jia, X. Meng and W. Wang, *Processes*, 2021, **9**, 871.
20 H. R. Zhao, J. H. Ding and H. B. Yu, *Ind. Eng. Chem. Res.*, 2018, **57**, 14096–14105.
21 A. Nadeem and M. A. Raza, *J. Pak. Int. Chem. Eng.*, 2021, **49**, 85–96.
22 A. Yadav, N. Bulakh, A. Gupta, N. Sikder and A. K. Sikder, *Anal. Methods*, 2017, **9**, 3141–3150.
23 J. Wu, A. Huang, W. Cao, X. Gao and Z. Chen, *J. Mater. Chem. A*, 2025, **13**, 1221–1229.
24 A. R. Deshmukh, P. K. Chaturvedi, S. Y. Lee, W. Y. Park and B. S. Kim, *ACS Sustainable Chem. Eng.*, 2022, **10**, 9573–9583.
25 Y. Shi, L. M. Song, Y. Liu, T. T. Wang, C. X. Li, J. P. Lai and L. Wang, *Adv. Energy Mater.*, 2024, **14**, 2402046.
26 D. Y. Chung, P. P. Lopes, P. F. B. D. Martins, H. Y. He, T. Kawaguchi, P. Zapol, H. You, D. Tripkovic, D. Strmcnik, Y. S. Zhu, S. Seifert, S. Lee, V. R. Stamenkovic and N. M. Markovic, *Nat. Energy*, 2020, **5**, 550.
27 Q. Jiang, S. H. Wang, C. R. Zhang, Z. Y. Sheng, H. Y. Zhang, R. H. Feng, Y. M. Ni, X. A. Tang, Y. C. Gu, X. H. Zhou, S. Lee, D. Zhang and F. Song, *Nat. Commun.*, 2023, **14**, 7418.
28 W. Zhan, H. Y. Wang, J. L. Gao, X. M. Tang, X. R. Zhu, Y. H. Xiao, X. Y. Sun, W. Gao and H. Yin, *Small Struct.*, 2023, **4**, 2300167.
29 H. B. Tao, Y. Xu, X. Huang, J. Chen, L. Pei, J. Zhang, J. G. Chen and B. Liu, *Joule*, 2019, **3**, 1498–1509.
30 V. T. T. Phan, Q. P. Nguyen, B. Wang and I. J. Burgess, *J. Am. Chem. Soc.*, 2024, **146**, 4830–4841.
31 X. Chen, X. Xu, Y. Cheng, H. Liu, D. Li, Y. Da, Y. Li, D. Liu and W. Chen, *Small*, 2024, **20**, 2303169.
32 L. Li, G. W. Zhang, C. H. Zhou, F. Lv, Y. J. Tan, Y. Han, H. Luo, D. W. Wang, Y. X. Liu, C. S. Shang, L. Y. Zeng, Q. Z. Huang, R. J. Zeng, N. Ye, M. C. Luo and S. J. Guo, *Nat. Commun.*, 2024, **15**, 4974.
33 Q. Z. Qian, X. Y. He, Z. Y. Li, Y. X. Chen, Y. F. Feng, M. Y. Cheng, H. K. Zhang, W. T. Wang, C. Xiao, G. Q. Zhang and Y. Xie, *Adv. Mater.*, 2023, **35**, 2300935.

34 C. Andronescu, S. Seisel, P. Wilde, S. Barwe, J. Masa, Y. T. Chen, E. Ventosa and W. Schuhmann, *Chem. – Eur. J.*, 2018, **24**, 13773–13777.
35 P. L. Zhai, C. Wang, Y. Y. Zhao, Y. X. Zhang, J. F. Gao, L. C. Sun and J. A. Hou, *Nat. Commun.*, 2023, **14**, 1873.
36 X. Cui, Y. X. Ding, F. Y. Zhang, X. Cao, Y. Guo, L. C. Sun and B. B. Zhang, *Nat. Chem.*, 2025, **18**, 120–127.
37 S. S. Zhao, Q. Dang, A. Q. Cao, M. G. Sendeku, H. Liu, J. Peng, Y. M. Fan, H. Li, F. M. Wang, Y. Kuang and X. M. Sun, *ACS Nano*, 2025, **19**, 8773–8785.